Pleural macrophages translocate to the lung during infection to promote improved influenza outcomes

James P Stumpff II[1], Sang Yong Kim[2], Adriana Forero[3], Andrew Nishida[3], Yael Steuerman[4], Irit Gat-Viks[4], Meera G Nair[2], Juliet Morrison[1]

[1]Department of Microbiology and Plant Pathology, University of California, Riverside, CA, USA

[2]Division of Biomedical Sciences, School of Medicine, University of California, Riverside, CA, USA

[3]Department of Microbiology, University of Washington, Seattle, WA, USA

[4]Shmunis School of Biomedicine and Cancer Research, Faculty of Life Sciences, Tel Aviv University, Tel Aviv, 6997801, Israel

*Corresponding author: Juliet Morrison, Department of Microbiology and Plant Pathology, 900 University Avenue, University of California, Riverside, CA 92521, USA. 1-951-827-5368, jmorriso@ucr.edu

The authors have declared that no conflict of interest exists.

ABSTRACT

Seasonal influenza results in 3 to 5 million cases of severe disease and 250,000 to 500,000 deaths annually. Macrophages have been implicated in both the resolution and progression of the disease, but the drivers of these outcomes are poorly understood. We probed mouse lung transcriptomic datasets using the Digital Cell Quantifier algorithm to predict immune cell subsets that correlated with mild or severe influenza A virus (IAV) infection outcomes. We identified a novel lung macrophage population that transcriptionally resembled small serosal cavity macrophages and correlated with mild disease. Until now, the study of serosal macrophage translocation in the context of infections has been neglected. Here, we show that pleural macrophages (PMs) migrate from the pleural cavity to the lung after infection with pH1N1 A/California/04/2009 IAV. We found that the depletion of PMs increased morbidity and pulmonary inflammation. There were increased proinflammatory cytokines in the pleural cavity and an influx of neutrophils within the lung. Our results show PMs are recruited to the lung during IAV infection and contribute to recovery from influenza. This study expands our knowledge of PM plasticity and provides a new source of lung macrophages independent of monocyte recruitment and local proliferation.

37 **GRAPHICAL ABSTRACT**

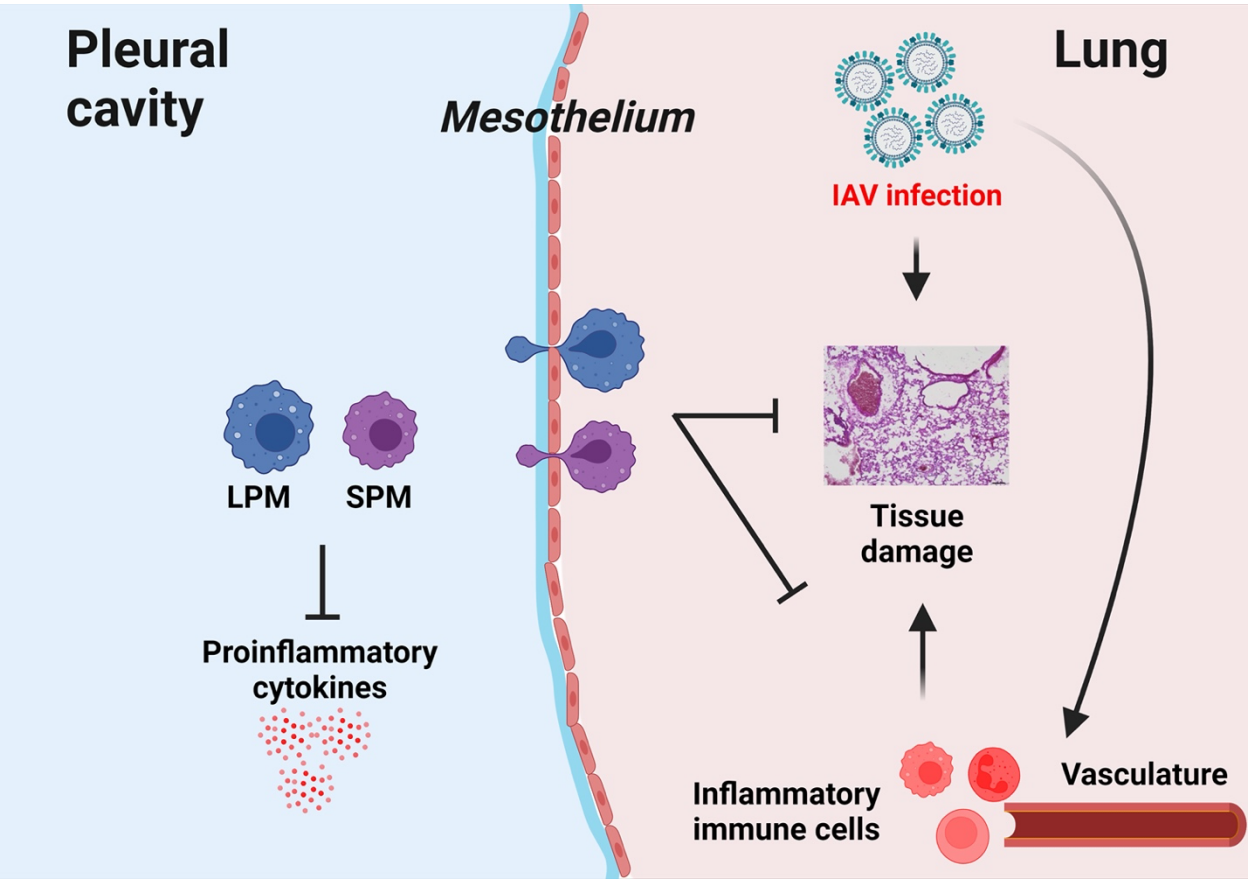

38

39 **INTRODUCTION**

40 IAV is responsible for seasonal epidemics and several pandemics that arose from
41 a lack of immunity and human-to-human transmission (1). Despite current vaccine
42 strategies, IAV remains a major public health concern. Patient outcomes of IAV infections
43 depend on the delicate balance between immune protection and immunopathology that
44 is orchestrated by innate immune responses and subsequent adaptive immunity (2).
45 Further investigation into IAV outcomes is needed to understand the resolution of viral
46 clearance and restoration of pulmonary homeostasis.

47 The host response to infection is an important determinant of influenza outcomes
48 (3-7). For example, severe influenza outcomes are associated with high levels of
49 proinflammatory cytokines and leukocytes in the lung (5, 7, 8). Patients hospitalized with
50 severe seasonal influenza infections have a sustained increase in monocytes (9), and
51 patients with severe avian influenza have elevated levels of inflammatory cytokines in
52 their acute-phase sera (10-12). Infection with highly pathogenic IAVs such as the 1918
53 virus and avian H5N1 virus leads to a massive recruitment of neutrophils and
54 inflammatory macrophages to the lungs of mice (3, 4). Depending on the virus strain,
55 mice may develop progressive pneumonia characterized by extensive neutrophilia,
56 hypercytokinemia, pulmonary edema, and reductions in alveolar gas exchange that are
57 reminiscent of acute respiratory distress (ARDS) in human patients (13-16). We
58 previously identified lung transcriptomic signatures that distinguished mild and severe
59 influenza outcomes in BALB/c mice infected with different IAV strains (17). A three-
60 pronged lung signature consisting of decreased expression of lipid metabolism and
61 coagulation genes and increased expression of proinflammatory cytokine genes had

62 developed in mice that had succumbed to infection, while a signature of increased
63 expression of lipid metabolism and coagulation genes and lower expression of
64 proinflammatory cytokine genes had developed in mice that recovered from infection (17).

65 Serous membranes support and protect the internal organs of all vertebrate
66 animals. Each serous membrane consists of two layers separated by a thin, fluid-filled
67 serosal cavity. The serosal cavity that envelops the lungs is called the pleural cavity, while
68 the cavities that surround the abdominal organs and the heart are known as the peritoneal
69 cavity and the pericardial cavity, respectively. Serosal cavities contain multiple immune
70 cells including innate B cells and T cells, but macrophages are the dominant cell
71 population. Serosal macrophages are divided into small and large macrophages based
72 on their cell size and surface marker expression. Small serosal macrophages are
73 $MHCII^{+}F4/80^{-}$ and constitute ~10% of serosal macrophages, while large serosal
74 macrophages are $MHCII^{-}F4/80^{+}$ and comprise ~90% of serosal macrophages (18-20).
75 Serosal macrophages have been implicated in organ health. For example, postoperative
76 gastrointestinal dysmotility can be ameliorated in mice by inhibiting peritoneal
77 macrophage functions (21). Furthermore, large peritoneal macrophages enter the liver to
78 promote wound healing in mouse models of sterile liver damage and dextran sulfate
79 sodium (DSS)-induced intestinal colitis (22, 23), while large pericardial macrophages
80 enter the heart to improve immune responses after myocardial infarction (24). However,
81 small serosal macrophages have not been studied in diseases of the visceral organs, and
82 serosal macrophages have never been studied in the context of viral infection.

83 In this manuscript, we use a systems biology approach as well as traditional “wet
84 lab” techniques to identify a new lung macrophage population that originates in the pleural

85 cavity and promotes recovery from influenza. To achieve this, we combined lung
86 transcriptomic datasets to identify and confirm transcriptomic signatures that distinguish
87 mild and severe influenza outcomes in mice. We then used a tissue deconvolution
88 algorithm known as Digital Cell Quantifier (DCQ) to convert lung transcriptomic data into
89 predictions of immune cell changes that precede different disease outcomes (25). We
90 found that DCQ accurately predicted known cell population dynamics that occurred during
91 influenza infection *in vivo*, and further predicted a lung cell population that transcriptionally
92 resembled small serosal macrophages and whose numbers positively correlated with
93 recovery from influenza.

94 We then used flow cytometry and microscopy to show that fluorescently-labeled
95 PMs migrate from the pleural cavity into the lung after infection with a seasonal influenza
96 virus strain, A/California/04/2009 (Cal09), after viral clearance has occurred and recovery
97 has been initiated. We further show that depleting PMs leads to increased virus-induced
98 weight loss and a longer recovery time. In addition, PM depletion causes increased
99 inflammatory cytokine levels in the pleural cavity and increased neutrophil infiltration in
100 the lung.

101 To our knowledge, we are the first to show that PMs translocate to the lung during
102 IAV infection, and that PMs are important for the resolution of IAV-induced lung disease.
103 We demonstrate the utility of our systems approach for discovering of immune cells
104 subsets that correlate with mild and severe disease outcomes. Furthermore, our findings
105 position the pleural cavity as an important contributor to lung homeostasis and the host
106 response to pneumonia.

RESULTS

Host response differences in expression of inflammatory, metabolic, cell cycle and tissue repair genes distinguish influenza disease outcomes.

Previously, we identified a gene expression signature in the mouse lung that could distinguish severe and mild influenza (17). We sought to expand our gene expression analysis to a wider range of influenza disease outcomes by including intermediate disease outcomes such as moderate weight loss and severe weight loss with subsequent recovery. Therefore, we integrated transcriptional data from our study (17) with data from an independent study of similar design (26). A description of the two studies and their combined weight loss outcomes are shown (**Figures 1A and 1B**). We restricted our analysis to those differentially-expressed (DE) genes that had a log fold change of 2 or more with an adjusted p-value cut-off of 0.05. When DE genes were clustered based on their biweight midcorrelation (bicor) across samples, six gene expression modules were identified and assigned unique colors (**Figure 1C**). We then used Ingenuity Pathway analysis (IPA) to assign functional categories to the genes within each module. The red module was enriched for genes in inflammation-associated pathways such as “Granulocyte adhesion and diapedesis” and “Crosstalk between dendritic cells and natural killer cells”. The increased induction of red module transcripts was associated with increased weight loss. The orange module, which had a unique expression pattern, was enriched for genes involved in lipid metabolism (“LXR/RXR activation” and “FXR/RXR activation” pathways) and coagulation. Upregulation of genes in this module on any day post infection in dataset GSE36328 or on day 3 post infection in dataset GSE54048 was associated with survival. Thus, expression patterns of genes within the red and orange

130 modules support our previous observation of perturbations in inflammation, lipid

131 metabolism, and coagulation signaling gene expression (17).

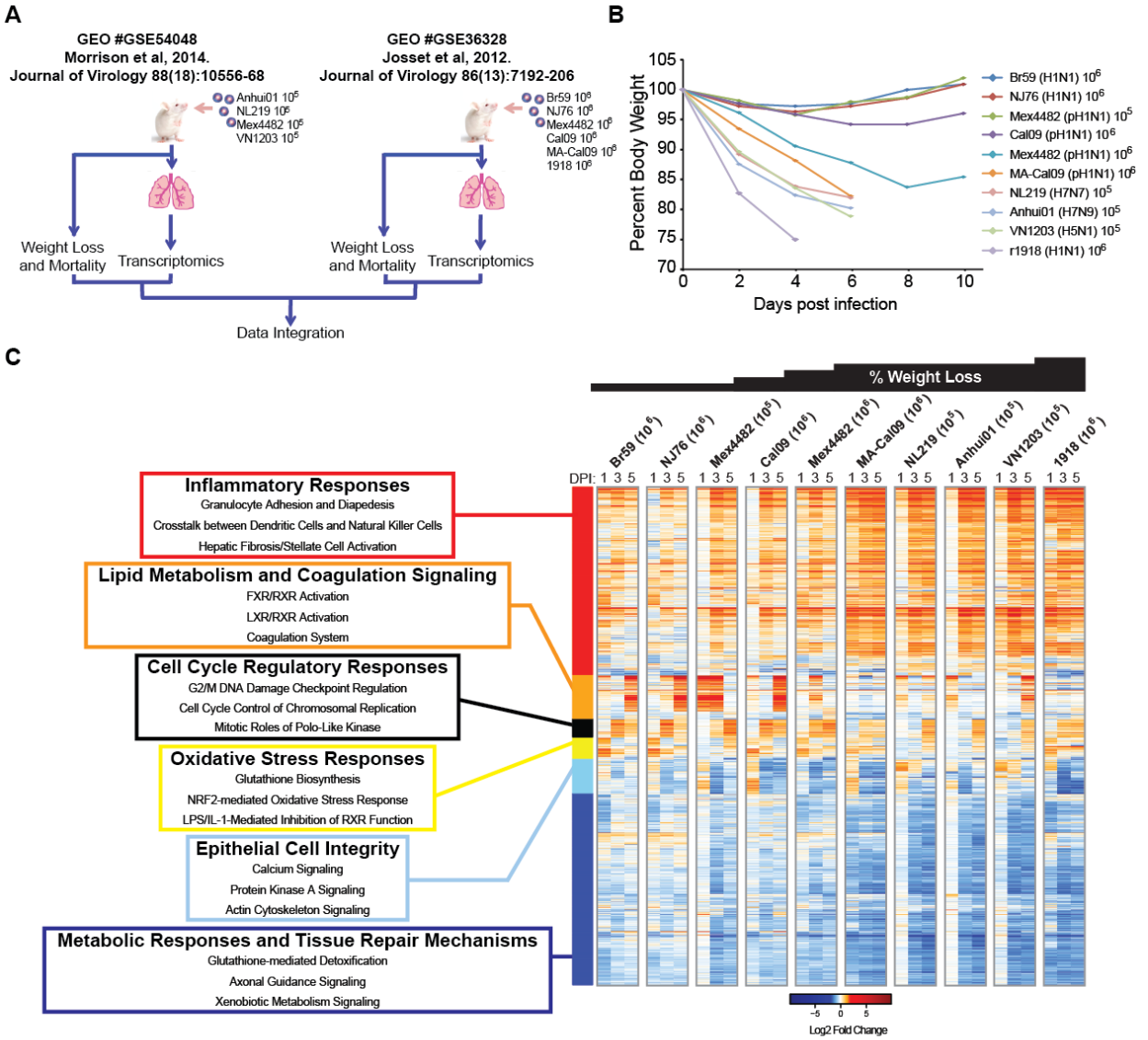

Figure 1. Different influenza disease outcomes are distinguished by host response differences in expression of inflammatory, metabolic, cell cycle and tissue repair genes. (A) Schematic showing the integration of BALB/C mouse data from GSE54048 and GSE36328. Experimental data were combined to produce (B) a combined weight loss dataset and a combined transcriptional dataset. (C) Hierarchical clustering of differential gene expression in murine lungs infected with influenza virus. Biweight midcorrelation clustering of 6012 genes that were found to be differentially expressed in any one condition (infection and time). Heatmap represents average gene expression intensity. Genes shown in red were upregulated and genes shown in blue were downregulated relative to uninfected lungs.

132 We then characterized the genes in the other four expression modules. The yellow
133 module, which contained genes involved in oxidative stress responses, did not have an
134 obvious pattern that related to weight loss or mortality. The sky-blue module, which
135 contained calcium and actin cytoskeleton signaling genes, also lacked a pattern with
136 regards to weight loss and mortality. Interestingly, upregulation of black module genes on
137 day 3 post infection was associated with infection by H1N1 viruses, but this upregulation
138 was unrelated to weight loss or mortality. The black module contained mitosis and cell
139 cycle control genes. The downregulation of genes in the dark-blue module, which was
140 enriched for tissue repair mechanisms and metabolic response genes, was associated
141 with increased weight loss. We hypothesized that this signature resulted from differential
142 activation or infiltration of immune cells in the lungs of mice that recovered versus those
143 that succumbed to IAV infection.
144
145 **Several immune cell types are predicted to correlate with influenza disease**
146 **severity.**
147 To identify immune cell populations that were potentially associated with the weight
148 loss and mortality outcomes, we employed a tissue deconvolution method known as
149 DCQ. The DCQ algorithm compares the gene expression profiles from 207 different
150 immune cells with whole organ transcriptional data to predict the quantities of immune
151 cells within a complex organ (25). This method utilizes a panel of genes encoding cell
152 surface markers that are commonly used for flow cytometry, and whose transcript and
153 protein levels are concordant (25). We took the populations measured by DCQ and used
154 linear regression to identify the cell populations whose numbers were most highly

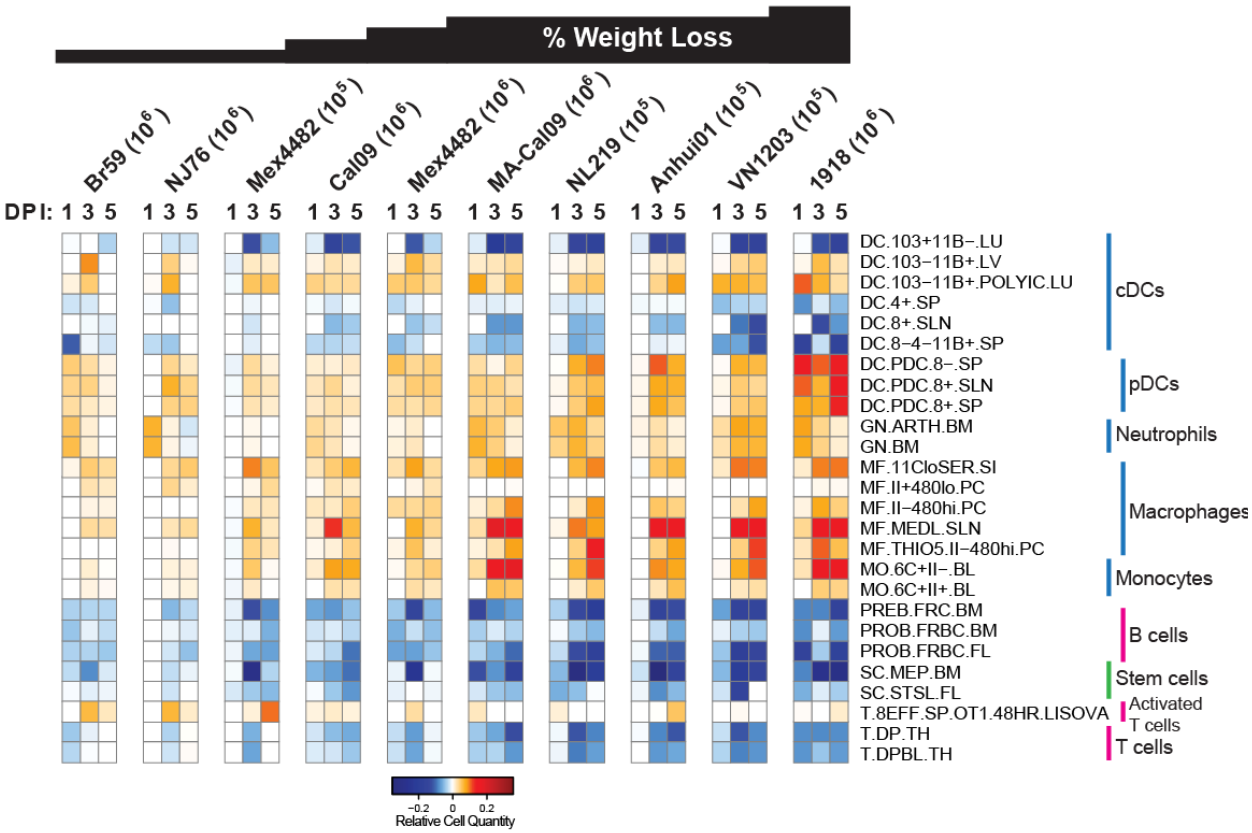

Figure 2. Digital cell quantifier identified immune cell subsets that predict disease severity or recovery across independent experiments. We surveyed the *in vivo* dynamics across time and viral strains using digital cell quantifier (DCQ; http://dcq.tau.ac.il). Linear regression models revealed distinct immune cell populations predicted to drive disease morbidity as defined by weight loss following influenza virus infection. The heatmap represents the relative quantity of cell types with significant relationships ($p < 0.05$) between that cell type on at least one day to the weights on at least one day after filtering for observations where data for at least 8 samples were available.

155 associated with weight loss in infected animals. We identified 26 cell types that were
156 positively or negatively correlated with influenza outcomes (**Figure 2**). Loss of stem cell
157 populations as well as lymphoid cells such as immature B and T cells and effector $CD8^+$
158 T cells was associated with increased weight loss. An increase in monocytes,
159 plasmacytoid dendritic cells (pDCs) and granulocytes was associated with increased
160 weight loss. Though increases in several conventional dendritic cell (cDC) and MF
161 populations were associated with increased weight loss and death, the presence of other
162 cDC and MF populations were associated with mild disease and recovery. For example,

163 decreases in CD103$^+$ cDCs (DC.103$^+$11B$^-$.LU) were associated with increased morbidity
164 and mortality. The presence of cells resembling MHCII$^+$F4/80^{lo} peritoneal MFs
165 (MF.II$^+$480^{lo}.PC) were associated with mild disease.
166
167 **Immune cell predictions are conserved across multiple transcriptomic datasets.**
168 To further bolster the tissue deconvolution predictions, we subjected two additional
169 microarray datasets to DCQ. In Shoemaker *et al.* (GSE63786), C57BL/6 mice were
170 infected with 10^5 PFU of Cal09 or VN1203, and monitored over the course of 7 days (27)
171 (**Figure S1A**). Lungs from VN1203-infected mice were found to have higher viral loads
172 and more pathology than lungs from Cal09-infected mice (27). In McDermott *et al.*
173 (GSE33263), C57BL/6 mice were infected with 10^2, 10^3 or 10^4 PFU VN1203 (28) (**Figure**
174 **S1B**). Higher inoculation titers led to increased weight loss and mortality (28). When
175 GSE63786 and GSE33263 were run through the DCQ algorithm, we found that the 26
176 cell types identified from the BALB/c datasets (**Figure 2**) largely showed a similar pattern
177 in the C57BL/6 data (**Figures S1C and S1D**). As with the BALB/c mice, an increase in
178 monocytes and granulocytes was associated with increased tissue pathology and weight
179 loss in C57BL/6 mice (**Figures S1C and S1D**). Loss of stem cell populations, immature
180 B and T cells and effector CD8$^+$ T cells was also associated with increased weight loss.
181 Again, the presence of cells resembling MHCII$^+$F4/80^{lo} peritoneal macrophages was
182 associated with mild disease (**Figures S1C and S1D**). The only prediction that did not
183 hold across the 4 datasets was that for pDC populations. Higher pDC numbers were
184 associated with severe disease in BALB/c mice (**Figure 2**) but were associated with mild
185 disease in C57BL/6 mice (**Figure S1**).

186 **Flow cytometry validates DCQ predictions.**

187 DCQ accurately identified cell population dynamics that have been shown to occur
188 during IAV infection *in vivo* (**Figures 2** and **S1**). For example, $CD103^{+}CD11b^{-}$ dendritic
189 cell numbers decrease post infection, modeling what occurs *in vivo* when they exit the
190 lung and traffic to the draining lymph nodes to present antigen to $CD8^{+}$ T cells (29, 30).

191 To further emphasize the value of our approach, we conducted *in vivo* experiments
192 to confirm some of the predictions. BALB/c mice were infected intranasally with 10^4
193 pH1N1 A/California/09 (Cal09) virus to induce mild disease or 10^4 H1N1 A/Puerto
194 Rico/1934 (PR8) virus to induce severe disease. Control mice received PBS intranasally.
195 We isolated, stained, and subjected lung cells to flow cytometry on day 3 post infection.
196 We validated the prediction that more neutrophils and $Ly6C^{+}$ monocytes were recruited
197 to the lung during severe disease (**Figure S2**) as has been described before (4, 9, 14, 31,
198 32).

199

200 **Influenza virus infection promotes the recruitment of pleural macrophages to the**
201 **lung.**

202 Our data thus far supported the idea of a $MHCII^{+}F4/80^{lo}$ macrophage population
203 that originates in a serosal cavity and is present in the lungs of mice that recover from
204 influenza. Since the macrophage populations of the pleural and peritoneal cavities are
205 analogous (18, 20), and the pleural cavity envelopes the lung, we hypothesized that the
206 $MHCII^{+}F4/80^{lo}$ lung macrophages predicted by DCQ originated in the pleural cavity.
207 Though CD11b, CD115, F4/80 and MHCII are sufficient for distinguishing the two pleural

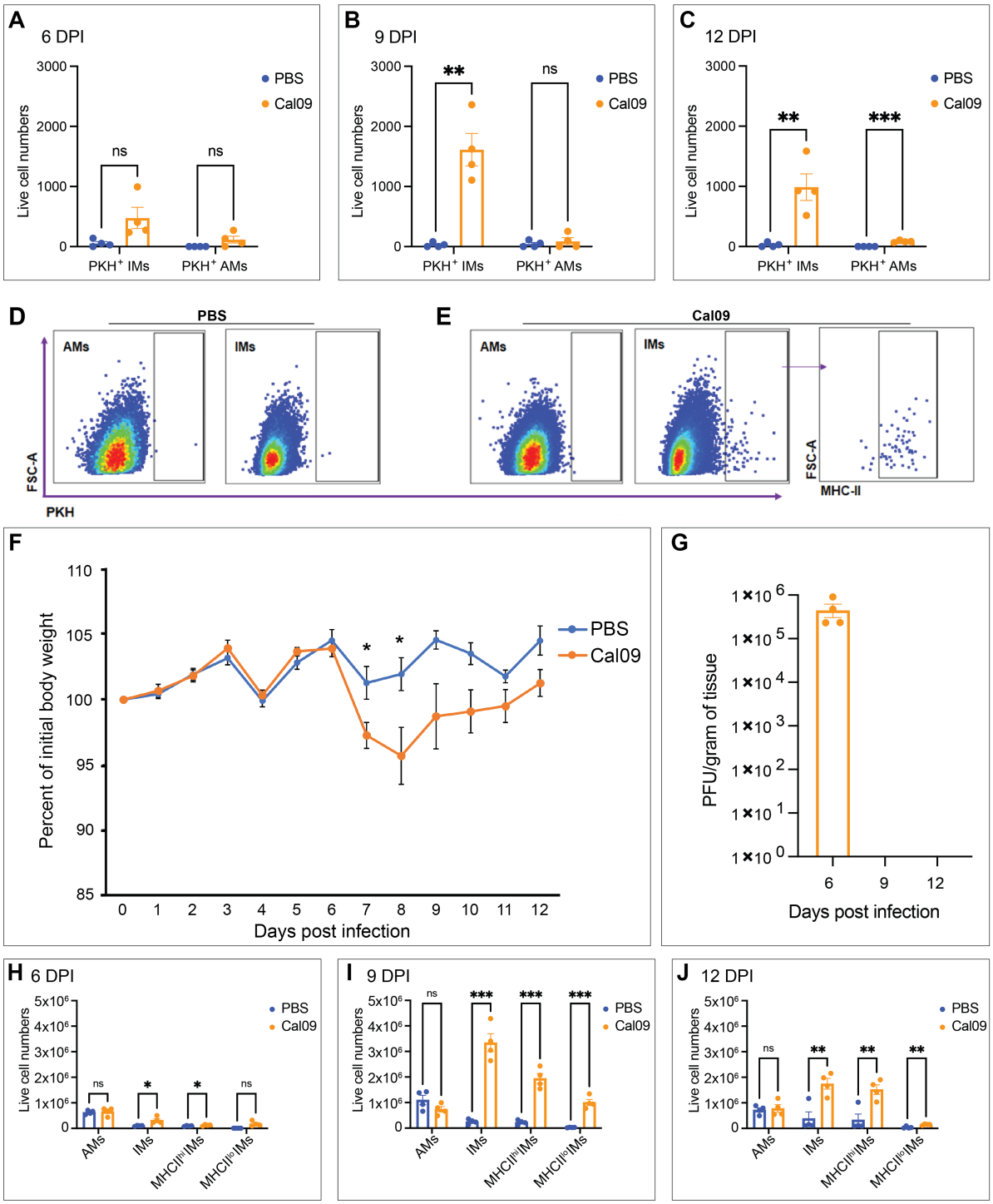

Figure 3. Influenza virus infection promotes the recruitment of pleural macrophages to the lung. BALB/c mice were intrapleurally injected with PKH26PCL dye one day before they were intranasally infected with 10^2 Cal09 virus or mock-infected with PBS as a control. (A-C) Quantification of live cell numbers of PKH$^+$ AMs and IMs in Cal09- or mock-infected mice. (D) Representative flow plots of PBS control mice. (E) Representative flow plots of Cal09 infected mice. (F) Representative growth curve of Cal09-infected versus PBS control mice. (G) Virus titers from lungs of mice in (F). (H-J) Quantification of live cell numbers of AMs and IMs in Cal09- or mock-infected mice. Data shown as mean ± SEM (n=4 from each group, *P<0.05, **P<0.01, ***P<0.001, Student's t-test). AM = alveolar macrophage (MerTK$^+$CD64$^+$SiglecF$^+$CD11b$^-$); IM = interstitial macrophage (MerTK$^+$CD64$^+$CD11b$^+$SiglecF$^-$).

208 macrophage (PM) populations, these markers are insufficient for distinguishing the

209 various macrophage populations in the lung. To circumvent issues with lung macrophage
210 identification, we focused instead on the potential origin of the novel lung population. PMs
211 were labeled *in vivo* by injecting a red phagocyte-specific dye (PKH26PCL) into the
212 pleural cavities of mice 1 day prior to infection. When mice were infected intranasally with
213 10^2 PFU of Cal09, PKH26PCL-labelled cells accumulated in the lung (**Figure 3**).
214 Translocated PMs were detected in the lungs on days 6, 9, and 12 post infection, but
215 more accumulation of the PKH^+ PMs occurred on 9 and 12 days post infection when
216 compared to the uninfected controls (**Figures 3A-E**). Flow cytometry gating strategies to
217 distinguish pleural and lung macrophage subpopulations are outlined in **Figures S3** and
218 **S4**.

219 PKH^+ cells in the lung were $CD64^+MerTK^+SiglecF^-CD11b^+$, which are
220 phenotypically like interstitial macrophages (IMs) (**Figure 3E**). A smaller pool of PMs did
221 phenotypically resemble $CD64^+MerTK^+SiglecF^+CD11b^-$ alveolar macrophages (AMs)
222 (**Figure 3E**). Heterogeneity amongst IMs has been researched in multiple studies (33-
223 35). One way of distinguishing them is based on their expression on MHCII. We found
224 that the majority of PKH^+ lung cells resembled $MHCII^+$ IMs (**Figure 3E).** Accumulation of
225 this $MHCII^+CD64^+MerTK^+SiglecF^-CD11b^+$ population that had originated in the pleural
226 cavity only occurred once animals began to regain weight and after they had cleared virus
227 from their lungs (**Figures 3F-G**). We also observed an overall increase in the total number
228 of IMs in the lung during IAV infection (**Figures 3H-J**).

229 To establish the location of the PKH^+ PMs in the lung, frozen lung sections were
230 immunostained and imaged by fluorescence microscopy 9 days post infection (**Figure**
231 **4A**). PKH^+ PMs in the lung are detected near the mesothelium (shown by the white dotted

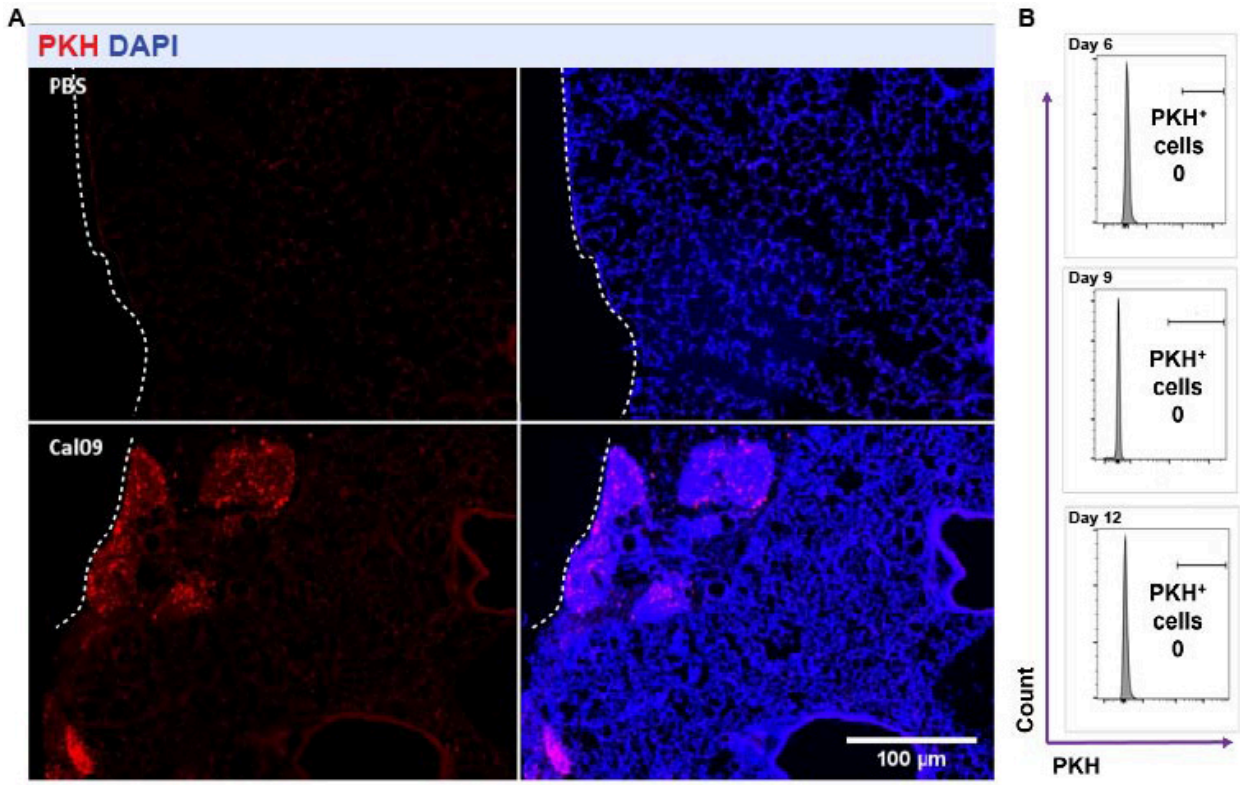

Figure 4. PMs localize near the mesothelium. (A) Representative fluorescent images of BALB/c naïve and Cal09-infected lungs harvested 9 days post infection. PMs were labeled *in vivo* with PKH26PCL dye (red) and counterstained with DAPI (blue). The mesothelium is depicted by the white dotted line (n = 3-7 from each group). (B) Flow cytometry of blood harvested from mice that had been intrapleurally injected with PKH26PCL dye then infected with Cal09 on days 6, 9 and 12 post infection.

line) and within regions of dense DAPI signal (**Figure 4A).** No PKH$^+$ PMs were detected in the PBS mock-infected control group. To determine whether the migration of PMs occurs through the vasculature, immune cells were isolated from blood on 6, 9, and 12 days post infection. Flow cytometric analysis showed no PKH$^+$ PMs in the blood from either the infected or the control group indicating that the labeled PMs had trafficked through the mesothelium (**Figure 4B)**.

240 **Pleural macrophage depletion leads to increased weight loss and slower recovery**
241 **from IAV infection.**

242 Previous studies have shown evidence for a role of cavity macrophages in models
243 of liver, heart and intestinal injury, showcasing differences in recruitment, wound repair,
244 and weight loss (22-24, 36). Another study suggested a role for PMs in bacterial clearance
245 in bacterial pneumonia (37). However, no study to date has investigated the role of PMs
246 in viral infection. To test whether PMs affect influenza outcomes, we depleted PMs by
247 injecting clodronate liposomes (CLL)
248 into the pleural cavities of mice 1 day
249 prior to infection with Cal09 virus. Flow
250 cytometry confirmed PMs were
251 depleted 24 hours after injection
252 (**Figure S5**), and up to 14 days after
253 injection. PM-depleted mice lost more
254 weight compared to the PBS
255 liposomes (PBSL)-injected control
256 mice (**Figure 5A**). However, we noted
257 no statistical differences in H&E-
258 stained lungs (**Figure S6A**) that had
259 been scored for airway thickening,
260 alveolar destruction, and vascular
261 inflammation on 9 days post infection

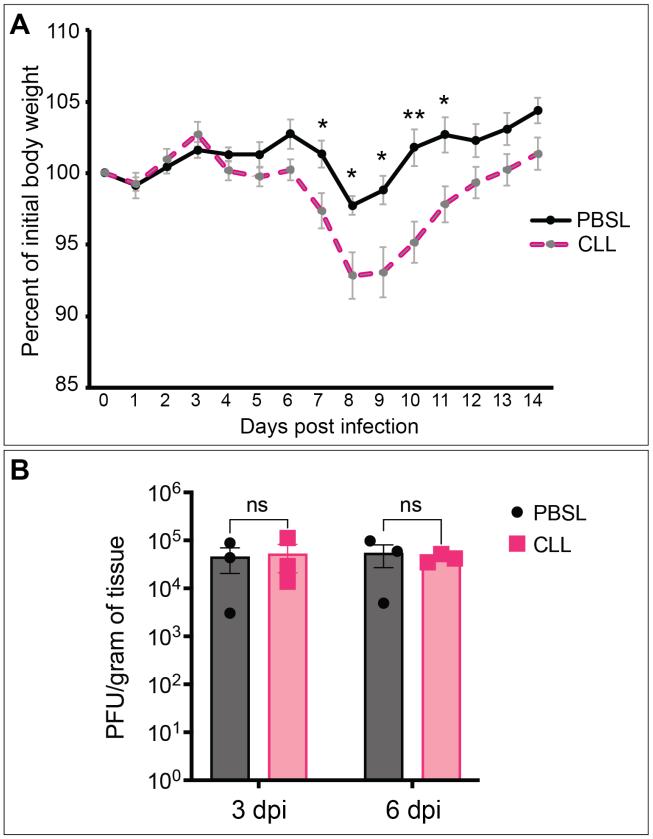

Figure 5. PM depletion increases disease severity without impacting viral titers. BALB/c mice received an intrapleural injection of CLL or PBSL one day before infection with 10^2 PFU of Cal09. (A) Weight loss was tracked over 14 days post infection in both CLL-injected and PBSL-injected groups (n=10 per group). (B) Virus titers from lungs of mice (n=3 per group). Data shown as mean ± SEM (*P<0.05, **P<0.01, ***P<0.001, ****P<0.0001, Student's t-test).

262 (**Figure S6B**). Lungs viral loads were unaffected by PM depletion (**Figure 5B**).

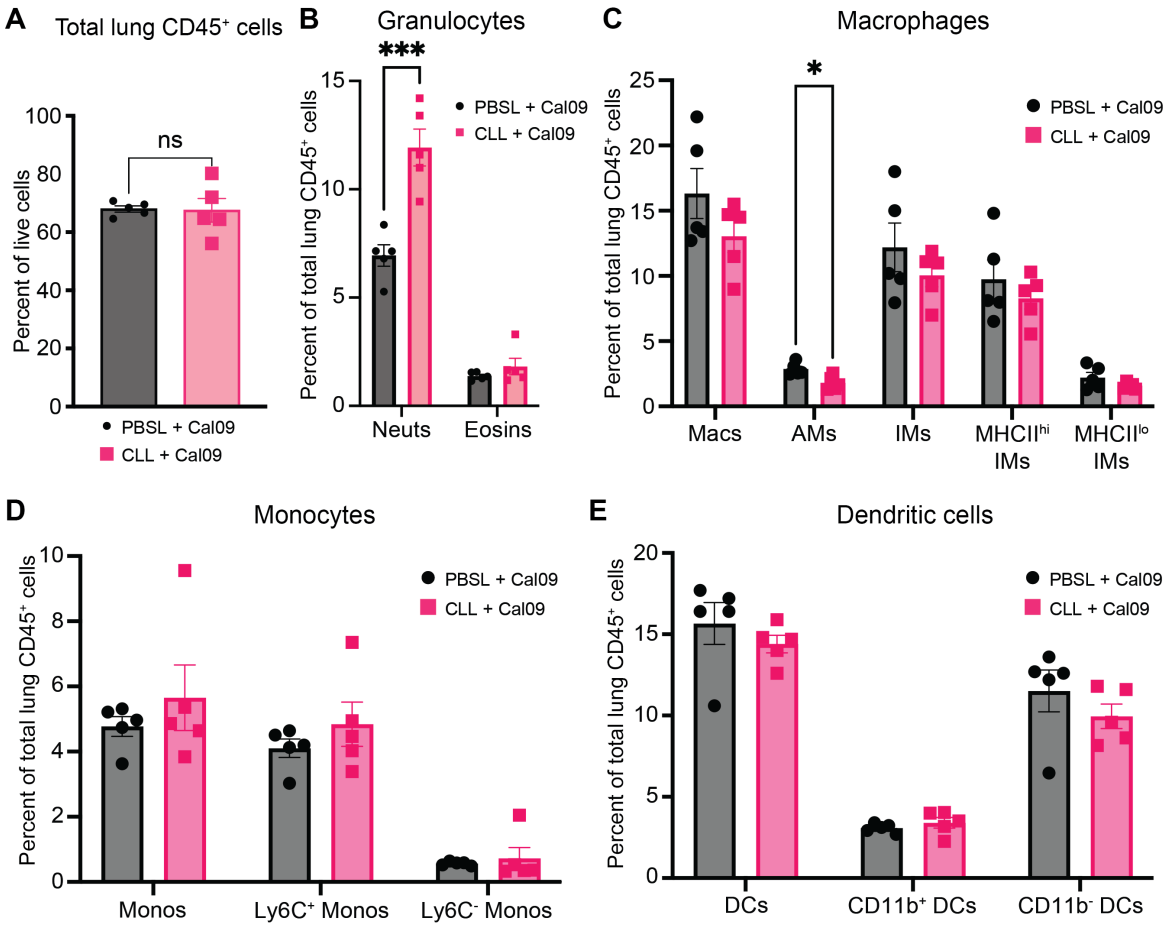

Figure 6. PM depletion increases neutrophil infiltration in the lung on day 9 post infection. BALB/c mice received an intrapleural injection of CLL or PBSL one day before infection with 10^2 PFU of Cal09, and lungs were isolated for flow cytometry on day 9 post infection. (A) Flow cytometric analysis of lung leukocytes ($CD45^+$), (B) neutrophils ($Ly6G^+CD11b^+$) and eosinophils ($CD11b^+SiglecF^+$), (C) *left to right,* macrophages ($CD64^+MerTK^+$) were divided into alveolar macrophages ($SiglecF^+CD11b^-$) and interstitial macrophages ($CD11b^+SiglecF^-$), which were further divided into two IM subsets ($MHCII^{hi/lo}$), (D) monocytes ($CD64^{lo}$) and two subpopulations ($Ly6C^{+/-}$), (E) dendritic cells ($CD11c^+MHCII^+CD24^+$) and two subpopulations ($CD11b^{+/-}$). Data shown as mean ± SEM (n=5 from each group, *P<0.05, **P<0.01, ***P<0.001, ****P<0.0001, Student's t-test). Neuts = neutrophils, eosins = eosinophils, macs = macrophages, AMs = alveolar macrophages, IMs = interstitial macrophages, monos = monocytes, DCs = dendritic cells

263 Since PM depletion led to more IAV-induced weight loss, we asked whether we
264 would see increased inflammation in the lungs of PM-depleted mice. By measuring the
265 number of $CD45^+$ cells in the lung, we found that the number of total leukocytes in the
266 lungs of PM-deficient and PM-sufficient mice were the same (**Figure 6A**). However, when

267 we looked at individual leukocyte populations, we found that CLL-treated mice had a
268 significantly higher percentage of neutrophils than PBSL-treated mice did on day 9 post
269 infection (**Figure 6B**). Our flow cytometry gating strategy for distinguishing lung leukocyte
270 populations is outlined in **Figure S7**. There were fewer AMs in CLL-treated mice (**Figure**

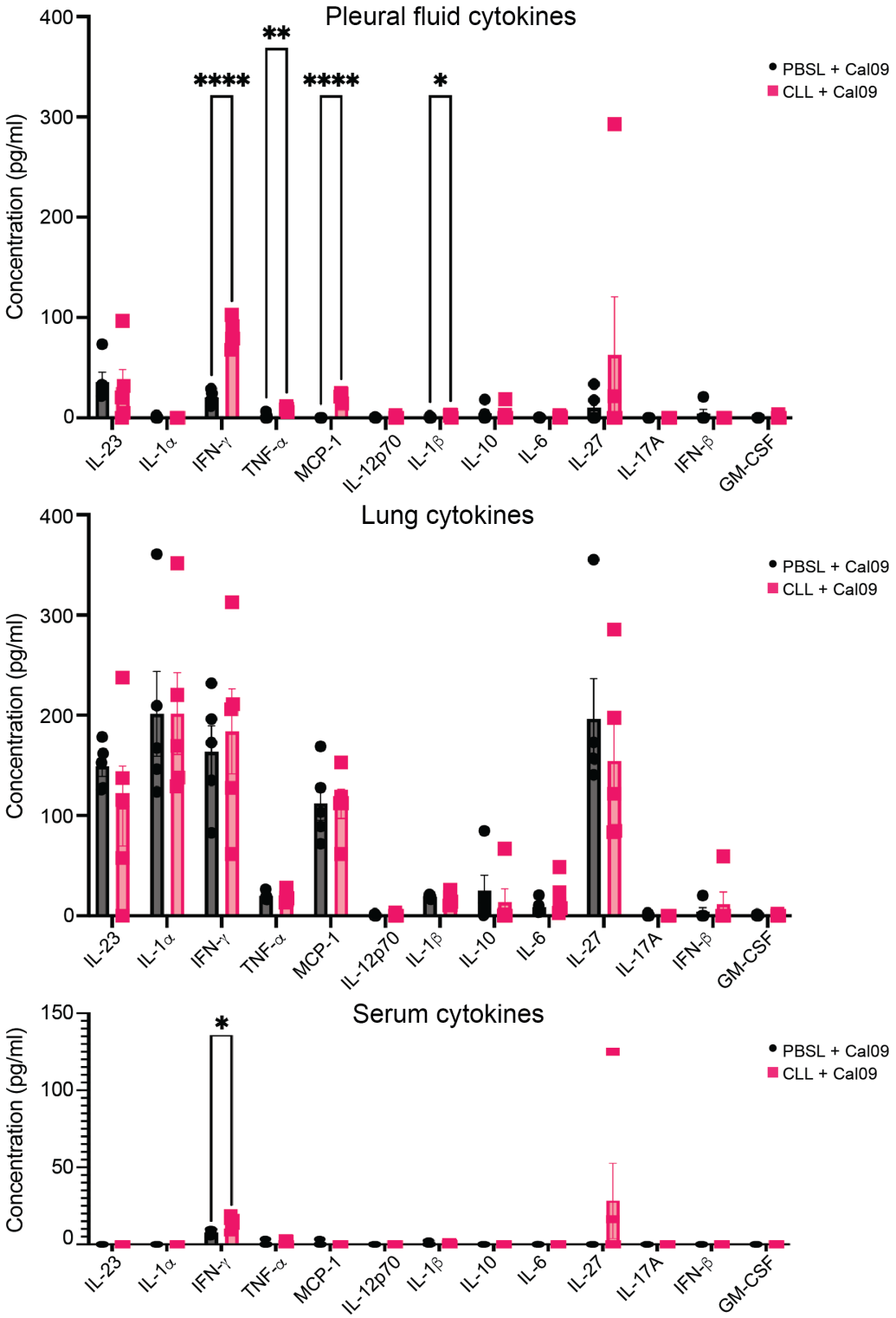

Figure 7. PM depletion leads to more proinflammatory cytokines in the pleural cavity on day 9 post infection. BALB/c mice received an intrapleural injection of CLL or PBSL one day before infection with 10^2 PFU of Cal09, and pleural fluid, lungs and sera were isolated on day 9 post infection. Cytokines from (A) pleural fluid, (B) lung homogenate, and (C) serum. Data shown as mean ± SEM (n=5 from each group, *P<0.05, **P<0.01, ***P<0.001, ****P<0.0001, Student's t-test)

271 **6C**). There were also fewer interstitial macrophages in CLL-treated mice albeit not

272 statistically significant (**Figure 6B**). No significant differences were observed in monocyte
273 and dendritic cell subsets (**Figure 6D-E**). Additionally, PM depletion led to increased
274 pleural cavity inflammation indicated by increased proinflammatory cytokines: interferon-
275 gamma (IFN-γ), tumor necrosis factor alpha (TNF-α) and monocyte chemoattractant
276 protein-1 (MCP-1) (**Figure 7A**). However, no proinflammatory cytokines were increased
277 in the lung between the infected groups (**Figure 7B**) though PM-depletion caused an
278 increase in serum IFN-γ levels in response to lung IAV infection at that time point (**Figure**
279 **7C**).
280

281 **DISCUSSION**

282 The impact of serosal macrophages on visceral organs has been an understudied
283 area of research. However, a few key studies have described migration of serosal
284 macrophages into visceral organs. These foundational studies focused on sterile injury or
285 inflammation of the liver, heart, and intestine (22-24). Here, we identified a previously
286 unrecognized role for PMs in influenza. We found that IAV infection triggers the
287 recruitment of mature macrophages from the pleural cavity, across the mesothelial layer,
288 and into the lung. PMs are recruited after the clearance of viral infection and when
289 restoration of homeostasis is critical. We observed this by labeling PMs via intrapleural
290 injection of PKH26PCL prior to IAV infection then measuring their translocation using flow
291 cytometry and immunofluorescence (**Figures 3** and **4**). A recent study defined one
292 population of IMs as nerve- and airway-associated macrophages, which express MHCII
293 and proliferate rapidly after IAV infection (38). Our data are supportive of this; we
294 observed a robust increase in the numbers of IMs, most of which are an MHCII^{hi}
295 subpopulation that peaked at 9-days post infection. We show that PMs that translocate
296 to the lung contribute to this MHCII^{hi} IM pool (**Figure 3**).

297 Our results differ from those of a recent study that described only surface
298 accumulation of pleural and peritoneal macrophages after organ injury, and did not
299 identify a role for serosal macrophages in tissue repair or regeneration (36). This
300 difference may be explained by the timepoints used for observation. We visualized PM
301 translocation at late timepoints–during the resolution phase–of a seasonal IAV infection
302 model and showed that PMs affect disease severity. Ablating PMs one day prior to

303 infection led to increased weight loss and neutrophil influx in the lungs of IAV-infected
304 mice.

305 While we were preparing this manuscript, Bénard *et al*. described increased
306 bacterial burden and mortality upon PM depletion in a mouse model of bacterial
307 pneumonia (37). Unlike in Bénard *et al*., where bacterial burdens increased upon PM
308 depletion and resulted in increased mortality, we saw increased disease severity without
309 differences in viral titers between PM-depleted and control groups after IAV infection.
310 Additionally, we showed that PMs traffic to the lung after IAV infection, while they did not
311 report PM translocation.

312 An important feature of our study was the use of a systems approach to generate
313 hypotheses. We identified signatures that distinguished mild and severe disease
314 outcomes in mice by combining lung transcriptomic data from two IAV mouse infection
315 studies. We then used tissue deconvolution and linear regression to screen immune
316 populations from the ImmGen database that could be driving differences in infection
317 outcomes. Though there is a great deal of heterogeneity amongst lung macrophage
318 populations (19, 20, 33-35, 39), the DCQ algorithm accurately predicted the presence of
319 a population resembling small serosal macrophages that accumulated only in the lungs
320 of animals that survived IAV infection. This prediction was foundational and served as an
321 important tool for identifying a novel immune cell population in our system. Nevertheless,
322 there are limits to tissue deconvolution approaches. Many macrophage populations from
323 different organs share similar phenotypic markers which make it difficult to predict the
324 origin of immune cell populations. In our case, the uniqueness of the small peritoneal
325 macrophage transcriptome in ImmGen was an asset to our predictions and subsequent

326 analyses. As such, characterizing additional immune populations of the serosal cavities
327 and other unique niches will be useful for future predictions.

328 PMs are important immunomodulators that impact the recovery of IAV-infected
329 mice by decreasing pleural space inflammation and lung neutrophil infiltration (**Figure 6**).
330 Tissue resident macrophages have been shown to "cloak" proinflammatory debris to
331 contain neutrophil-driven tissue damage and inflammation (40). Furthermore, attenuation
332 of neutrophil influx in IAV infection can improve survival without impacting viral titers (31).
333 Thus, it is feasible that recruited PMs may play a role in masking damage signals to
334 prevent neutrophil infiltration. Pulmonary inflammation can lead to pleural inflammation,
335 which is associated with increased mortality in pneumonia patients and in patients
336 hospitalized with pleural effusion (41, 42). IFN-γ levels were higher in both pleural fluid
337 and sera of IAV-infected, PM-depleted mice (**Figure 7**). IFN-γ deficiency has been shown
338 to decrease susceptibility to lethal infection by increasing activation of group II innate
339 lymphoid cells (ILC2s) (43). We also saw increased MCP-1 in the pleural cavity, and this
340 has been shown to contribute to pleurisy and pleural effusion in carrageenan-induced
341 pleurisy (44).

342 The pleural cavity may serve as a reservoir for other immune cells that can migrate
343 to the lung. B1a cells, another pleural cavity immune cell population, have important roles
344 in bacterial pneumonia and were shown to migrate to the lung after LPS challenge (45).
345 Furthermore, during IAV infection, pleural cavity B1a cells have important pulmonary
346 responses and are suggested to migrate to infected lungs (46). Whether other pleural
347 cavity cell populations can migrate to the lung has not been determined, but when we
348 looked at other innate immune cell populations, we did not detect PKH^+ cells.

349 The role of the pleural cavity in other viral infections and secondary bacterial
350 infections remains poorly understood. However, meta-analyses of SARS-CoV-2-infected
351 patients showed that pleural effusion was associated with poorer COVID-19 prognoses
352 (47). Similar observations have been seen in patients infected with IAV and/or bacteria
353 (41, 42, 48-50). Additionally, pleural space inflammation can provide protection against
354 bacterial lung infection (37). Following viral infection, patients are left more vulnerable to
355 subsequent pneumonia, but PMs may limit inflammation after infection and decrease
356 susceptibility to pneumonia. There is therefore a need for more research into pleural
357 cavity function in the context of lung infection. Altogether, we show that PMs migrate to
358 the lung during IAV infection and play a role in limiting disease severity by modulating
359 inflammatory responses both in the pleural cavity and in the lung. Selectively targeting
360 PMs could serve as a strategy for treating severe influenza and other lung and pleural
361 diseases. Future studies to understand how PM translocation and plasticity are regulated
362 are warranted.
363

364 **METHODS**

365 **Gene expression analysis**

366 The primary transcriptomic data sets GEO Accession number GSE54048,
367 GSE36328, GSE63786 and GSE33263 (17, 26-28) were extracted and quantile
368 normalized using the “normalizeBetweenArrays” method available in the “limma” package
369 of the R suite (51), and adjusted for batch effects using ComBat software (52). Expression
370 across each sample was normalized to the average expression of study- and time-
371 matched mocks. Differential gene expression following viral infection was determined by

372 deriving the ratio of expression between the average gene expression of influenza virus-
373 infected replicates to the average of time-matched mock-infected samples applying a
374 linear model fit using the “limma” package (51). Criteria for differential expression (DE)
375 were an absolute log-fold change of 2 and an adjusted *P* value of <0.05, calculated by
376 Benjamini-Hochberg correction. Functional analysis of DE genes was done using
377 Ingenuity Pathway Analysis (IPA; Ingenuity Systems) using a right-tailed Fisher exact test
378 with a threshold of significance set at *P* value of 0.05.
379
380 **Computational measurement of immune cell subsets**
381 Immune cell dynamics during the course of infection were surveyed using the
382 Digital Cell Quantifier (DCQ) algorithm as previously described (25). Genome-wide gene
383 expression was normalized for each infection relative to the average of the time-matched
384 mock, and a log 2 transformation applied. Each gene expression entry was divided by the
385 standard deviation across test samples. Analysis of relative cell quantity was run with
386 three repeats and a lambda minimum of 0.2. For each of the 207 cell types in DCQ and
387 their three time points on day 1, day 3, and day 5, we used a simple linear model to
388 estimate the relationship between the sample’s expression for that cell type on that day
389 to the weights on days 2, 4, 6, 8, 10, and 12.
390
391 **Viruses**
392 pH1N1 A/California/04/2009 and H1N1 A/Puerto Rico/8/1934 viruses were a kind
393 gift from Dr. Adolfo García-Sastre (Icahn School of Medicine at Mount Sinai). Virus stocks

394 were propagated in 8-day-old embryonated eggs (Charles River Laboratories) and titrated
395 by plaque assays on MDCK cells.
396
397 **Mouse experiments**
398 Female BALB/c mice, 8 to 12 weeks old, were purchased from Jackson Laboratory
399 (Bar Harbor, ME) and used for all mouse experiments.
400 Mice were injected intrapleurally, under isoflurane anesthesia, with 100 μl of 10μM
401 PKH26PCL fluorescent dye (Sigma Aldrich) one day before virus infection. In other
402 experiments, mice were injected intrapleurally, under isoflurane anesthesia, with 50 μl of
403 clodronate liposomes or PBS control liposomes (Encapsula Nano Sciences) one day
404 before virus infection. Mice were challenged intranasally, under isoflurane anesthesia,
405 with 50 μl PBS containing 10^2 or 10^4 PFU of pH1N1 A/California/04/2009 or H1N1
406 A/PR/8/1934 viruses, or mock challenged with PBS alone. Lungs were collected and
407 homogenized in 1 ml PBS and stored at −80 °C until virus titration. Viral titers were
408 measured by plaque assays on MDCK cells.
409
410 **Tissue homogenization**
411 Lungs were harvested at indicated timepoints and washed in PBS before being
412 placed in 2-ml tubes containing 1 ml 1X PBS, 3% FBS, and 1mM EDTA, and one ceramic
413 bead (MP Biomedicals). Lung tissue was homogenized with the FastPrep-24 bead beater
414 at 7.00 speed/s twice for 20 seconds each then placed on ice for 5 min and repeated.
415 After homogenization, samples were centrifuged at 21,300xg for 15 min. Supernatant was
416 aliquoted into new tubes and stored at -80°C.

417

418 **Plaque assay**

419 MDCK cells were seeded in 6-well culture plates and incubated at 37°C in 5% CO_2
420 for 24 hours. 10-fold serial dilutions were prepared in a solution containing 1x PBS, 0.21%
421 BSA, 1% Pen/Strep, and 1% Ca/Mg. Cells were washed once with PBS before adding
422 200 ml of the serial dilutions. Plates were incubated at 37°C and were rocked side-to-side
423 and forward-to-back every 15 minutes to distribute virus inoculum over the monolayer of
424 cells for 1 hour. TPCK-treated trypsin (1 mg/ml) was added at a 1:1000 ratio to a
425 supplemented 2X DMEM (2X DMEM, 2% Pen/Strep, 0.42% BSA, 20 mM HEPES, 0.24%
426 $NaHCO_3$, 0.02% DEAE-Dextran) before mixing with 1.5% Oxoid Agar at a 1:1 ratio. 2 ml
427 of the agar overlay was added to each well and allowed to cool for 15 min at room
428 temperature before transferring to the 37°C incubator. Plates were incubated for 96 hours.
429 After incubation, plates were fixed with 1 ml of a 3.7% formaldehyde solution and
430 incubated for 10 minutes to neutralize infectious virus. Overlay was flicked out with a
431 spatula and stained for 20 min with crystal violet (0.095% crystal violet, 2.8% ethanol,
432 19% methanol). Plates were rinsed in tap water and plaques were counted to determine
433 viral titers.

434

435 **Cytokine and chemokine detection**

436 Cytokines and chemokines from pleural fluid, serum, and lung were quantified
437 using the LEGENDplex™ (Biolegend, 740150) mouse inflammation panel (13-plex). All
438 samples were analyzed on a NovoCyte Quanteon and data was analyzed using
439 LEGENDplex™ software (Biolegend).

440

441 **Preparation of cell suspensions, flow cytometry and cell sorting**

442 For isolation of pleural cavity cells, the pleural cavity was washed twice with 500
443 μl sterile cold PBS. The fluid was centrifuged at 500xg for 5 min at 4°C and resuspended
444 in RBC lysis buffer (Sigma, R7757) for 5 min at room temperature. Fluorescence-
445 activated cell sorting (FACS) buffer (1x PBS, 3% FBS and 2 mM EDTA) was added to
446 stop the lysis and the fluid was centrifuged at 500xg for 5 min at 4°C and resuspended in
447 FACS buffer.

448 For isolation of immune cells from blood, tubes were prepared with 1 ml of 4%
449 sodium citrate. Blood was transferred to these tubes to prevent clotting and mixed well. 1
450 ml of FACS buffer was then added. Tubes were underlaid with 1 ml Histopaque (Sigma,
451 10771-6X100ML) using a Pasteur pipette. Samples were centrifuged at 400xg for 20 min
452 at room temperature. The interface was collected and transferred to a new 15 ml conical
453 tube and washed with 10 ml of FACS buffer to remove Histopaque. After RBC lysis,
454 samples were resuspended in FACS buffer.

455 For isolation of immune cells from lungs, lungs were removed and collected in a
456 15-ml centrifuge tube containing 10 ml FACS buffer and placed on ice. Lungs were
457 transferred to a petri dish and macerated with razor blades. 3 ml of lung digestion buffer
458 containing HBSS (Lonza, BE10-508F), 5% FBS, 1 mg/ml collagenase A (Sigma, 2674-
459 500mg), and 0.05 mg/ml DNase I (Roche, 11284932001) was added and transferred to
460 a new 15-ml centrifuge tube. Lungs were incubated at 37°C shaking for 1 hour. In the last
461 15 minutes of the digestion, lungs were syringed with a 1 ml syringe and 18g needle
462 approximately 20 times. To stop digestion, 10 ml of FACS buffer was added and spun at

463 400xg for 4 min at 4°C. After lysing RBCs, cells were resuspended in FACS buffer and
464 pushed through a 70-μm cell strainer.

465 Cavity cells, blood cells and lung single-cell suspensions were washed with PBS
466 and resuspended in PBS containing live/dead fixable aqua dye (Invitrogen, L34957), and
467 incubated at room temperature for 15 min. Cells were then washed and resuspended with
468 FACS buffer. Fc receptors were blocked with anti-CD16/32 Fc block antibody (BD
469 Biosciences, 553142) and Rat IgG then stained with primary antibodies. The antibodies
470 used for staining were as follows: MerTK AF488 (BioLegend, 151504), CD115 PE-CF594
471 (Biolegend, 135528), I-A/I-E PerCP (BioLegend, 107624), Ly6c PE/Cy7 (BioLegend,
472 128018), CD64 APC (BioLegend, 139306), CD11b APC/Fire™ 750 (BioLegend, 101262),
473 SiglecF BV421 (BD Biosciences, 565934), CD11c BV605 (117333), F4/80 BV650
474 (BioLegend, 123149), CD24 PE-CF594 (BD Biosciences, 562477), Ly6G PE (BioLegend,
475 127607), CD45 Alexa Fluor 700 (BioLegend, 103127). Cells were stained for 30 min at
476 4°C then washed with FACS buffer. Afterwards, the cells were fixed in 2%
477 paraformaldehyde (PFA) for 20 min at 4°C and resuspended in FACS buffer. Samples
478 were processed on an LSRII (BD Biosciences) or NovoCyte Quanteon (Agilent) and
479 analyzed with FlowJo software (BD Biosciences). For cell sorting, samples were treated
480 similarly, but without fixation, and sorted on a MoFlo Astrios EQ Cell Sorter (Beckman
481 Coulter). FACS buffer used for cell sorting was HBSS without calcium or magnesium and
482 supplemented with 3% FBS, 2mM EDTA and 25mM HEPES. Cells were dispensed into
483 sorting buffer with 4x the amount of FBS.

484

485 **Tissue preparation for immunofluorescence and hematoxylin and eosin staining**

486 Mice were sacrificed at the indicated time points. Lungs were inflated with 1 ml of
487 a solution containing 1 part 4% PFA/30% sucrose and 2 parts of optimal cutting
488 temperature compound (OCT) media (Fisher Scientific). Inflated lungs were tied off and
489 stored in 4% PFA/30% sucrose at 4°C overnight. The following day lungs were transferred
490 to 30% sucrose and stored overnight at 4°C. Lungs were then blocked in OCT on dry ice
491 and stored at -80°C. Tissue was sectioned at 10-20 μm on a cryostat. For histological
492 assessment tissues were stained with hematoxylin and eosin. Slides were assessed in a
493 double-blind manner.
494 For immunofluorescence, slides were mounted with ProLong Glass Antifade
495 Mountant with NucBlue (Invitrogen, P36981). Images were acquired using a Keyence BZ-
496 X710 fluorescent microscope. Image analysis was conducted with two images per
497 section, two sections per slide, two slides per animal with n = 5 animals per condition.
498 Images were analyzed on ImageJ.
499
500 ***Ex vivo* labeling of macrophages with PKH26PCL dye**
501 Sorted cell populations were washed twice with serum-free media then
502 resuspended in 500 μl diluent from the PKH26PCL-1KT. In a separate tube, PKH dye
503 solution was prepared at a 5 μM concentration in 500 μl of PKH dye. Dye solution was
504 then added to resuspended cells and incubated for 5 minutes and then washed three
505 times with media containing serum.
506
507 **Statistics**

508 All results were presented as the mean ± SEM. R and GraphPad Prism 9.4 were
509 used for statistical analyses. The analyses were conducted using Student's t test for
510 comparison between two groups and one-way ANOVA was used to test comparisons
511 between multiple groups (*P < 0.05, **P < 0.01, ***P < 0.001, ****P < 0.0001, and ns for
512 not significant).
513
514 **Study approval**
515 All experiments with mice were performed in accordance with protocols approved
516 by the University of California Riverside Institutional Animal Care and Use Committee.
517

518 **AUTHOR CONTRIBUTIONS**

519 JM conceived and designed the research study. JM, AF, and AN conducted the
520 transcriptomic analyses. IGV and YS provided guidance on DCQ. JM and JPS designed
521 the *in vitro* and *in vivo* experiments. JPS, JM, and SYK conducted the *in vitro* and *in vivo*
522 experiments. JPS and JM analyzed the *in vitro* and *in vivo* experimental data. JM, JPS,
523 MGN, and SYK contributed to data interpretation. JM and JPS wrote the manuscript. All
524 authors read and approved the final manuscript.

525

526 **ACKNOWLEDGEMENTS**

527 We thank Maudry Laurent-Rolle, Deborah Spector, Mafalda De Arrabida, Roksana
528 Shirazi, and Xueyan Xu for critical feedback on this manuscript. We thank Adolfo García-
529 Sastre for providing pH1N1 A/California/04/2009 and H1N1 A/Puerto Rico/8/1934
530 influenza A viruses as well as MDCK cells. The graphical abstract was created with
531 BioRender.com.

532

533 **FUNDING SOURCES**

534 This research was supported by University of California, Riverside funds (to JM) and a
535 Regents Faculty Fellowship, University of California (to JM).

536

537 **CONFLICTS OF INTEREST**

538 The authors have declared that no conflict of interest exists.

539 **REFERENCES**
540
541

542 1. Horimoto T, and Kawaoka Y. Influenza: lessons from past pandemics, warnings from
543 current incidents. *Nature reviews Microbiology.* 2005;3(8):591-600.
544 2. Lamichhane PP, and Samarasinghe AE. The Role of Innate Leukocytes during Influenza
545 Virus Infection. *J Immunol Res.* 2019;2019:8028725.
546 3. Kash JC, Tumpey TM, Proll SC, Carter V, Perwitasari O, Thomas MJ, et al. Genomic
547 analysis of increased host immune and cell death responses induced by 1918 influenza
548 virus. *Nature.* 2006;443(7111):578-81.
549 4. Perrone LA, Plowden JK, Garcia-Sastre A, Katz JM, and Tumpey TM. H5N1 and 1918
550 pandemic influenza virus infection results in early and excessive infiltration of
551 macrophages and neutrophils in the lungs of mice. *PLoS Pathog.* 2008;4(8):e1000115.
552 5. Short KR, Kroeze EJ, Fouchier RA, and Kuiken T. Pathogenesis of influenza-induced acute
553 respiratory distress syndrome. *Lancet Infect Dis.* 2014;14(1):57-69.
554 6. Tisoncik JR, Korth MJ, Simmons CP, Farrar J, Martin TR, and Katze MG. Into the eye of
555 the cytokine storm. *Microbiology and molecular biology reviews : MMBR.* 2012;76(1):16-
556 32.
557 7. Writing Committee of the WHOCoCAoPI, Bautista E, Chotpitayasunondh T, Gao Z,
558 Harper SA, Shaw M, et al. Clinical aspects of pandemic 2009 influenza A (H1N1) virus
559 infection. *N Engl J Med.* 2010;362(18):1708-19.
560 8. Herold S, Becker C, Ridge KM, and Budinger GR. Influenza virus-induced lung injury:
561 pathogenesis and implications for treatment. *Eur Respir J.* 2015;45(5):1463-78.
562 9. Cole SL, Dunning J, Kok WL, Benam KH, Benlahrech A, Repapi E, et al. M1-like monocytes
563 are a major immunological determinant of severity in previously healthy adults with life-
564 threatening influenza. *JCI Insight.* 2017;2(7):e91868.
565 10. Chi Y, Zhu Y, Wen T, Cui L, Ge Y, Jiao Y, et al. Cytokine and chemokine levels in patients
566 infected with the novel avian influenza A (H7N9) virus in China. *J Infect Dis.*
567 2013;208(12):1962-7.
568 11. de Jong MD, Simmons CP, Thanh TT, Hien VM, Smith GJ, Chau TN, et al. Fatal outcome
569 of human influenza A (H5N1) is associated with high viral load and hypercytokinemia.
570 *Nat Med.* 2006;12(10):1203-7.
571 12. Wang Z, Zhang A, Wan Y, Liu X, Qiu C, Xi X, et al. Early hypercytokinemia is associated
572 with interferon-induced transmembrane protein-3 dysfunction and predictive of fatal
573 H7N9 infection. *Proc Natl Acad Sci U S A.* 2014;111(2):769-74.
574 13. Fukushi M, Ito T, Oka T, Kitazawa T, Miyoshi-Akiyama T, Kirikae T, et al. Serial
575 histopathological examination of the lungs of mice infected with influenza A virus PR8
576 strain. *PloS one.* 2011;6(6):e21207.
577 14. Narasaraju T, Yang E, Samy RP, Ng HH, Poh WP, Liew AA, et al. Excessive neutrophils and
578 neutrophil extracellular traps contribute to acute lung injury of influenza pneumonitis.
579 *Am J Pathol.* 2011;179(1):199-210.
580 15. Traylor ZP, Aeffner F, and Davis IC. Influenza A H1N1 induces declines in alveolar gas
581 exchange in mice consistent with rapid post-infection progression from acute lung injury
582 to ARDS. *Influenza Other Respir Viruses.* 2013;7(3):472-9.

583 16. Xu T, Qiao J, Zhao L, Wang G, He G, Li K, et al. Acute respiratory distress syndrome
584 induced by avian influenza A (H5N1) virus in mice. *Am J Respir Crit Care Med.*
585 2006;174(9):1011-7.
586 17. Morrison J, Josset L, Tchitchek N, Chang J, Belser JA, Swayne DE, et al. H7N9 and other
587 pathogenic avian influenza viruses elicit a three-pronged transcriptomic signature that is
588 reminiscent of 1918 influenza virus and is associated with lethal outcome in mice. *J*
589 *Virol.* 2014;88(18):10556-68.
590 18. Bain CC, Hawley CA, Garner H, Scott CL, Schridde A, Steers NJ, et al. Long-lived self-
591 renewing bone marrow-derived macrophages displace embryo-derived cells to inhabit
592 adult serous cavities. *Nat Commun.* 2016;7:ncomms11852.
593 19. Ghosn EE, Cassado AA, Govoni GR, Fukuhara T, Yang Y, Monack DM, et al. Two
594 physically, functionally, and developmentally distinct peritoneal macrophage subsets.
595 *Proc Natl Acad Sci U S A.* 2010;107(6):2568-73.
596 20. Kim KW, Williams JW, Wang YT, Ivanov S, Gilfillan S, Colonna M, et al. MHC II+ resident
597 peritoneal and pleural macrophages rely on IRF4 for development from circulating
598 monocytes. *J Exp Med.* 2016;213(10):1951-9.
599 21. Maehara T, Matsumoto K, Horiguchi K, Kondo M, Iino S, Horie S, et al. Therapeutic
600 action of 5-HT3 receptor antagonists targeting peritoneal macrophages in post-
601 operative ileus. *Br J Pharmacol.* 2015;172(4):1136-47.
602 22. Honda M, Kadohisa M, Yoshii D, Komohara Y, and Hibi T. Directly recruited GATA6 +
603 peritoneal cavity macrophages contribute to the repair of intestinal serosal injury. *Nat*
604 *Commun.* 2021;12(1):7294.
605 23. Wang J, and Kubes P. A Reservoir of Mature Cavity Macrophages that Can Rapidly
606 Invade Visceral Organs to Affect Tissue Repair. *Cell.* 2016;165(3):668-78.
607 24. Deniset JF, Belke D, Lee WY, Jorch SK, Deppermann C, Hassanabad AF, et al. Gata6(+)
608 Pericardial Cavity Macrophages Relocate to the Injured Heart and Prevent Cardiac
609 Fibrosis. *Immunity.* 2019;51(1):131-40 e5.
610 25. Altboum Z, Steuerman Y, David E, Barnett-Itzhaki Z, Valadarsky L, Keren-Shaul H, et al.
611 Digital cell quantification identifies global immune cell dynamics during influenza
612 infection. *Mol Syst Biol.* 2014;10:720.
613 26. Josset L, Belser JA, Pantin-Jackwood MJ, Chang JH, Chang ST, Belisle SE, et al. Implication
614 of inflammatory macrophages, nuclear receptors, and interferon regulatory factors in
615 increased virulence of pandemic 2009 H1N1 influenza A virus after host adaptation. *J*
616 *Virol.* 2012;86(13):7192-206.
617 27. Shoemaker JE, Fukuyama S, Eisfeld AJ, Zhao D, Kawakami E, Sakabe S, et al. An
618 Ultrasensitive Mechanism Regulates Influenza Virus-Induced Inflammation. *PLoS*
619 *Pathog.* 2015;11(6):e1004856.
620 28. McDermott JE, Shankaran H, Eisfeld AJ, Belisle SE, Neuman G, Li C, et al. Conserved host
621 response to highly pathogenic avian influenza virus infection in human cell culture,
622 mouse and macaque model systems. *BMC Syst Biol.* 2011;5:190.
623 29. Ballesteros-Tato A, Leon B, Lund FE, and Randall TD. Temporal changes in dendritic cell
624 subsets, cross-priming and costimulation via CD70 control CD8(+) T cell responses to
625 influenza. *Nat Immunol.* 2010;11(3):216-24.

626 30. Helft J, Manicassamy B, Guermonprez P, Hashimoto D, Silvin A, Agudo J, et al. Cross-
627 presenting CD103+ dendritic cells are protected from influenza virus infection. *J Clin*
628 *Invest.* 2012;122(11):4037-47.
629 31. Brandes M, Klauschen F, Kuchen S, and Germain RN. A systems analysis identifies a
630 feedforward inflammatory circuit leading to lethal influenza infection. *Cell.*
631 2013;154(1):197-212.
632 32. Lin KL, Suzuki Y, Nakano H, Ramsburg E, and Gunn MD. CCR2+ monocyte-derived
633 dendritic cells and exudate macrophages produce influenza-induced pulmonary immune
634 pathology and mortality. *J Immunol.* 2008;180(4):2562-72.
635 33. Chakarov S, Lim HY, Tan L, Lim SY, See P, Lum J, et al. Two distinct interstitial
636 macrophage populations coexist across tissues in specific subtissular niches. *Science.*
637 2019;363(6432).
638 34. Gibbings SL, Thomas SM, Atif SM, McCubbrey AL, Desch AN, Danhorn T, et al. Three
639 Unique Interstitial Macrophages in the Murine Lung at Steady State. *Am J Respir Cell*
640 *Mol Biol.* 2017;57(1):66-76.
641 35. Schyns J, Bai Q, Ruscitti C, Radermecker C, De Schepper S, Chakarov S, et al. Non-
642 classical tissue monocytes and two functionally distinct populations of interstitial
643 macrophages populate the mouse lung. *Nat Commun.* 2019;10(1):3964.
644 36. Jin H, Liu K, Tang J, Huang X, Wang H, Zhang Q, et al. Genetic fate-mapping reveals
645 surface accumulation but not deep organ invasion of pleural and peritoneal cavity
646 macrophages following injury. *Nat Commun.* 2021;12(1):2863.
647 37. Benard A, Podolska MJ, Czubayko F, Kutschick I, Klosch B, Jacobsen A, et al. Pleural
648 Resident Macrophages and Pleural IRA B Cells Promote Efficient Immunity Against
649 Pneumonia by Inducing Early Pleural Space Inflammation. *Front Immunol.*
650 2022;13:821480.
651 38. Ural BB, Yeung ST, Damani-Yokota P, Devlin JC, de Vries M, Vera-Licona P, et al.
652 Identification of a nerve-associated, lung-resident interstitial macrophage subset with
653 distinct localization and immunoregulatory properties. *Sci Immunol.* 2020;5(45).
654 39. Dick SA, Wong A, Hamidzada H, Nejat S, Nechanitzky R, Vohra S, et al. Three tissue
655 resident macrophage subsets coexist across organs with conserved origins and life
656 cycles. *Sci Immunol.* 2022;7(67):eabf7777.
657 40. Uderhardt S, Martins AJ, Tsang JS, Lammermann T, and Germain RN. Resident
658 Macrophages Cloak Tissue Microlesions to Prevent Neutrophil-Driven Inflammatory
659 Damage. *Cell.* 2019;177(3):541-55 e17.
660 41. Kookoolis AS, Puchalski JT, Murphy TE, Araujo KL, and Pisani MA. Mortality of
661 Hospitalized Patients with Pleural Effusions. *J Pulm Respir Med.* 2014;4(3):184.
662 42. Rosenstengel A. Pleural infection-current diagnosis and management. *J Thorac Dis.*
663 2012;4(2):186-93.
664 43. Califano D, Furuya Y, Roberts S, Avram D, McKenzie ANJ, and Metzger DW. IFN-gamma
665 increases susceptibility to influenza A infection through suppression of group II innate
666 lymphoid cells. *Mucosal Immunol.* 2018;11(1):209-19.
667 44. Lansley SM, Cheah HM, and Lee YC. Role of MCP-1 in pleural effusion development in a
668 carrageenan-induced murine model of pleurisy. *Respirology.* 2017;22(4):758-63.

669 45. Weber GF, Chousterman BG, Hilgendorf I, Robbins CS, Theurl I, Gerhardt LM, et al.
670 Pleural innate response activator B cells protect against pneumonia via a GM-CSF-IgM
671 axis. *J Exp Med.* 2014;211(6):1243-56.
672 46. Wang X, Ma K, Chen M, Ko KH, Zheng BJ, and Lu L. IL-17A Promotes Pulmonary B-1a Cell
673 Differentiation via Induction of Blimp-1 Expression during Influenza Virus Infection. *PLoS*
674 *Pathog.* 2016;12(1):e1005367.
675 47. Rathore SS, Hussain N, Manju AH, Wen Q, Tousif S, Avendano-Capriles CA, et al.
676 Prevalence and clinical outcomes of pleural effusion in COVID-19 patients: A systematic
677 review and meta-analysis. *J Med Virol.* 2022;94(1):229-39.
678 48. Dean NC, Griffith PP, Sorensen JS, McCauley L, Jones BE, and Lee YC. Pleural Effusions at
679 First ED Encounter Predict Worse Clinical Outcomes in Patients With Pneumonia. *Chest.*
680 2016;149(6):1509-15.
681 49. Kim YN, Cho HJ, Cho YK, and Ma JS. Clinical significance of pleural effusion in the new
682 influenza A (H1N1) viral pneumonia in children and adolescent. *Pediatr Pulmonol.*
683 2012;47(5):505-9.
684 50. Hasley PB, Albaum MN, Li YH, Fuhrman CR, Britton CA, Marrie TJ, et al. Do pulmonary
685 radiographic findings at presentation predict mortality in patients with community-
686 acquired pneumonia? *Arch Intern Med.* 1996;156(19):2206-12.
687 51. Ritchie ME, Phipson B, Wu D, Hu Y, Law CW, Shi W, et al. limma powers differential
688 expression analyses for RNA-sequencing and microarray studies. *Nucleic Acids Res.*
689 2015;43(7):e47.
690 52. Johnson WE, Li C, and Rabinovic A. Adjusting batch effects in microarray expression data
691 using empirical Bayes methods. *Biostatistics.* 2007;8(1):118-27.
692